Microbial Cell Factories

RESEARCH

Open Access

Sustainability of in vitro light-dependent NADPH generation by the thylakoid membrane of *Synechocystis* sp. PCC6803

Xiaomeng Tong[1], Eui-Jin Kim[2*] and Jeong K. Lee[1*]

Abstract

Background: NADPH is used as a reductant in various biosynthetic reactions. Cell-free bio-systems have gained considerable attention owing to their high energy utilization and time efficiency. Efforts have been made to continuously supply reducing power to the reaction mixture in a cyclical manner. The thylakoid membrane (TM) is a promising molecular energy generator, producing NADPH under light. Thus, TM sustainability is of major relevance for its in vitro utilization.

Results: Over 70% of TMs prepared from *Synechocystis* sp. PCC6803 existed in a sealed vesicular structure, with the F_1 complex of ATP synthase facing outward (right-side-out), producing NADPH and ATP under light. The NADPH generation activity of TM increased approximately two-fold with the addition of carbonyl cyanide-p-(trifluoromethoxy) phenylhydrazone (FCCP) or removal of the F_1 complex using EDTA. Thus, the uncoupling of proton translocation from the electron transport chain or proton leakage through the F_o complex resulted in greater NADPH generation. Biosilicified TM retained more than 80% of its NADPH generation activity after a week at 30°C in the dark. However, activity declined sharply to below 30% after two days in light. The introduction of engineered water-forming NADPH oxidase (Nox^m) to keep the electron transport chain of TM working resulted in the improved sustainability of NADPH generation activity in a ratio (Nox^m to TM)-dependent manner, which correlated with the decrease of singlet oxygen generation. Removal of reactive oxygen species (ROS) by catalase further highlighted the sustainable NADPH generation activity of up to 80% in two days under light.

Conclusion: Reducing power generated by light energy has to be consumed for TM sustainability. Otherwise, TM can generate singlet oxygen, causing oxidative damage. Thus, TMs should be kept in the dark when not in use. Although NADPH generation activity by TM can be extended via silica encapsulation, further removal of hydrogen peroxide results in an improvement of TM sustainability. Therefore, as long as ROS formation by TM in light is properly handled, it can be used as a promising source of reducing power for in vitro biochemical reactions.

Keywords: Thylakoid membrane, Reducing power, Sustainability, Nox, ROS, Biosilicification

Introduction

The thylakoid of cyanobacteria houses photosynthetic machinery. This membranous structure is composed of flattened sacs that are organized into stacks [1, 2]. Further, it is the site of light-dependent photosynthesis, harboring components required for electron transport involved in both linear electron flow (LEF) and cyclic electron flow (CEF) [3, 4]. LEF is utilized for the

*Correspondence: ejkim@nnibr.re.kr; jgklee@sogang.ac.kr

[1] Department of Life Science, Sogang University, Mapo, Shinsu 1, Seoul 121-742, Korea
[2] Microbial Research Department, Nakdonggang National Institute of Biological Resources, Gyeongsangbuk-do, Sangju-si 37242, Korea

generation of NADPH and ATP, whereas CEF is exclusively involved in ATP production [5, 6].

The main module for light-driven electron flow comprises the water-splitting complex, photosystem II (PS II), cytochrome b_6f (cyt b_6f), photosystem I (PS I), and electron carriers of plastoquinone (PQ) in the membrane, in addition to plastocyanin (PC) in the lumen [3, 4, 7, 8]. The phycobilisome (PBS) acts as a light-harvesting complex and transfers light energy to PS II [9]. Ferredoxin (Fd) is finally reduced and used as a substrate for ferredoxin-$NADP^+$ oxidoreductase (FNR) to form NADPH [10]. Meanwhile, the proton motive force (pmf) is formed across the TM, thus driving ATP production by ATP synthase.

The vesicular structure of the TM can be readily formed following isolation from phototrophic organisms. The TM from *Spinacia oleracea* was shown to generate NADPH and ATP under light and was used for CO_2 fixation and poly (3-hydroxybutyrate) production in vitro [11, 12]. TM from *Chlamydomonas reinhardtii* has also been used to study H_2 generation in vitro [13]. Thus, the TM represents a promising light-dependent energy generator for biochemical reactions in vitro. However, the limited in vitro durability of TMs limits their long-term utility [11, 12].

The sustainability of chromatophore membrane vesicles derived from the intracytoplasmic membrane of *Rhodobacter sphaeroides* has been improved by immobilization on streptavidin resin [14]. However, the use of resins in large quantities is not cost-effective. Recently, biosilicification has attracted a lot of attention, as some bacteria naturally form a silica shell that protects against environmental stress [15–17]. In this process, silicic acid is converted into polymerized silica under physiological conditions [18]. Over the past few decades, microorganism-coating biomimetic silica has been utilized on account of numerous merits. Silica coating not only preserves cell viability, but also offers a rigid protective layer against external stress [19–21]. The porous nature of silica-based shields enable cells to uptake necessary metabolites from the culture medium [22, 23]. Moreover, silica-mediated immobilization of enzymes facilitates their reusability without compromising stability [24]. Encapsulated proteins confined by silica shells are known to possess considerable resistance to acidic environment, digestive enzymes, and denaturing agents [25–27]. However, if the thickness of silica shell exceeds a certain limit, the movement of reactants across silica is restricted and would slow down the reaction [26].

The long-term exposure of TM to light may impair its biocatalyst activity, which could be ascribed to the unstable properties of the lipid bilayer [28] and reactive oxygen species (ROS)-induced oxidative damage to membrane lipids and proteins [29]. The redox poise of electron carriers must be maintained throughout electron transport during photosynthesis. Otherwise, a reduced carrier can liberate electrons to molecular oxygen to generate ROS [30, 31].

In this study, we sought ways to improve the sustainability of NADPH generation by TMs, since there are various other methods of producing ATP in vitro [32, 33]. Considering surface protection, biomimetic silicification was used to wrap up the TM and test whether it improves sustainability. Furthermore, ROS formation by the TM was examined during active light exposure. To provide cyclic conversion between NADPH and $NADP^+$, an engineered water-forming NADPH oxidase (Nox^m) was applied after introducing mutations to gain substrate preference for NADPH over NADH [34].

Materials and methods

Bacterial strains and growth conditions

Synechocystis sp. PCC6803 (hereafter referred to as *Synechocystis*) was grown at 30°C in BG-11 medium with 10 mM glucose, as previously described [35]. The culture broth was agitated at 110 rpm under 50 μmol m^{-2} s^{-1} white light. Cells for TM isolation were harvested at an OD_{730} in the range of 1.8–2.5. *Escherichia coli* was cultivated in Luria–Bertani (LB) broth [36]. Antibiotics were supplied as described hereafter when necessary [36]. Kanamycin (Km) and ampicillin (Ap) were added at 25 μg mL^{-1} and 50 μg mL^{-1} for *E. coli*, respectively. Gentamicin (Gm) was used at 30 μg mL^{-1} for both *Synechocystis* and *E. coli*. To induce protein expression, 1 mM IPTG was added to both strains. Anhydrotetracycline was used at 200 ng mL^{-1} for *E. coli*.

Plasmid construction

The plasmids used to determine the orientation of TMs were constructed by introducing a his_6-tag into the N-terminus of the β subunit and a strep-tag into the N-terminus of the c subunit of ATP synthase via PCR with primers harboring tag sequences. Briefly, a 1.5-kb fragment containing the β subunit (*atpB*) was PCR-amplified from *Synechocystis* genomic DNA using primers AtpB-F1 and AtpB-R1 (Additional file 1: Table S1). The resulting fragment was digested with *Bam*HI and *Eco*RI, followed by ligation into the *Bam*HI/*Eco*RI sites of pSL1211 [37] to generate pSL-AtpB (Table 1), which was expressed under the control of the IPTG-inducible *trc* promoter. A 246-bp DNA fragment containing the c subunit (*atpH*) was PCR amplified using primers AtpH-F and AtpH-R (Additional file 1: Table S1), digested with *Bam*HI and *Eco*RI, and ligated into the *Bam*HI/*Eco*RI sites of pSL1211 to yield pSL-AtpH (Table 1).

Table 1 Strains and plasmids used in this study

Strains/plasmids	Relevant characteristics	Reference/description
Strains		
E. coli		
DH5α*phe*	*phe*::Tn10*d*Cm of DH5α	[74]
S17-1	C600::RP4 2-(Tc::Mu)(Km::Tn7) *thi pro hsdR hsdM*$^+$ *recA*	[75]
BL21(DE3)	B F- *dcm ompT hsdS*($r_B^-m_B^-$) *gal* λ(ED3)	
Synechocystis sp. PCC 6803	Type strain	
Syn-AtpB	*Synechocystis* containing pSL-AtpB	This study
Syn-AtpH	*Synechocystis* containing pSL-AtpH	This study
Plasmids		
pSL1211	*ori* RSF1010, IPTG-inducible promoter; Gm^r	[37]
pSL-AtpB	pSL1211 + 1.5-kb *Bam*HI-*Eco*RI fragment containing *atpB*; Gm^r	This study
pSL-AtpH	pSL1211 + 246-bp *Bam*HI-*Eco*RI fragment containing *atpH*; Gm^r	This study
pASK-IBA3plus	*ori* f1, Ap^r; For expression of recombinant protein with C-terminal strep-tag	IBA Lifesciences
IBA-AtpA	pASK-IBA3plus + 1.5-kb *Bsa*I fragment containing *atpA*; Ap^r	This study
IBA-AtpB	pASK-IBA3plus + 1.5-kb *Bsa*I fragment containing *atpB*; Ap^r	This study
IBA-AtpD	pASK-IBA3plus + 558-bp *Bsa*I fragment containing *atpD*; Ap^r	This study
IBA-AtpE	pASK-IBA3plus + 498-bp *Bsa*I fragment containing *atpE*; Ap^r	This study
IBA-KatE	pASK-IBA3plus + 1.5-kb *Bam*HI-*Pst*I fragment containing *katE*; Ap^r	This study
pASK-IBA7plus	*ori* f1, Ap^r; For expression of recombinant protein with N-terminal strep-tag	IBA Lifesciences
IBA-FNR	pASK-IBA7plus + 1.2-kb *Bam*HI-*Pst*I fragment containing *petH*; Ap^r	This study
IBA-Fd	pASK-IBA7plus + 369-bp *Eco*RI-*Pst*I fragment containing *petF*; Ap^r	This study
IBA-ApcA	pASK-IBA7plus + 486-bp *Bam*HI-*Pst*I fragment containing *apcA*; Ap^r	This study
IBA-CpcA	pASK-IBA7plus + 489-bp *Bam*HI-*Pst*I fragment containing *cpcA*; Ap^r	This study
pGEX-4T-3	pBR322 *ori*, Ap^r; For expression of recombinant protein with N-terminal GST-tag	This study
pGEX-AtpC	pGEX-4T-3 + 498-bp *Eco*RI-*Xho*I fragment containing *atpC*; Ap^r	This study
pRSET-A	pBR322 *ori*, Ap^r; For expression of recombinant protein with N-terminal his_6-tag	Invitrogen
pRSET-Nox	pRSET-A + 1.3-kb *Bam*HI-*Pst*I fragment containing *noxV*; Ap^r	This study
pRSET-Nox178	pRSET-A + 1.3-kb *Bam*HI-*Pst*I fragment containing *noxG178R*; Ap^r	This study
pRSET-Nox178179	pRSET-A + 1.3-kb *Bam*HI-*Pst*I fragment containing *noxG178RL179R*; Ap^r	This study

A 1.5-kb DNA fragment containing ATP synthase subunit α (*atpA*) was PCR-amplified from *Synechocystis* genomic DNA using the primers AtpA-F and AtpA-R (Additional file 1: Table S1). The PCR product was digested with *Bsa*I and ligated into the *Bsa*I site of pASK-IBA3plus with a C-terminal strep-tag fusion to yield IBA-AtpA (Table 1).

A 1.5-kb DNA fragment containing ATP synthase subunit β (*atpB*) was PCR-amplified from *Synechocystis* genomic DNA using primers AtpB-F2 and AtpB-R2 (Additional file 1: Table S1). The PCR product was digested with *Bsa*I and ligated into the *Bsa*I site of pASK-IBA3plus with a C-terminal strep-tag fusion to yield IBA-AtpB (Table 1).

A 432-bp DNA fragment containing ATP synthase subunits γ (*atpC*) was PCR-amplified from *Synechocystis* genomic DNA using primers AtpC-F and AtpC-R (Additional file 1: Table S1). The resulting fragment was digested with *Eco*RI and *Xho*I, followed by ligation into the *Eco*RI/*Xho*I sites of pGEX-4T-3 with N-terminal GST-tag fusion to yield pGEX-AtpC (Table 1).

A 558-bp DNA fragment containing ATP synthase subunits δ (*atpD*) was PCR-amplified from *Synechocystis* genomic DNA using the primers AtpD-F and AtpD-R (Additional file 1: Table S1). The PCR product was digested with *Bsa*I and ligated into the *Bsa*I site of pASK-IBA3plus with a C-terminal strep-tag fusion to yield IBA-AtpD (Table 1).

A 498-bp DNA fragment containing ATP synthase subunit ε (*atpE*) was PCR-amplified from *Synechocystis* genomic DNA using primers AtpE-F and AtpE-R (Additional file 1: Table S1). The PCR product was digested with *Bsa*I and ligated into the *Bsa*I site of pASK-IBA3plus with a C-terminal strep-tag fusion to yield IBA-AtpE (Table 1).

A 1.2-kb fragment containing FNR (*petH*) was PCR-amplified from *Synechocystis* genomic DNA using primers FNR-F and FNR-R (Additional file 1: Table S1).

The PCR product was digested with *Bam*HI and *Pst*I, and ligated into the *Bam*HI/*Pst*I sites of pASK-IBA7plus to generate IBA-FNR (Table 1) with an N-terminal strep-tag fusion.

A 369-bp fragment containing Fd (*petF*) was PCR-amplified from *Synechocystis* genomic DNA using primers Fd-F and Fd-R (Additional file 1: Table S1). The PCR product was digested with *Eco*RI and *Pst*I, and ligated into the *Eco*RI/*Pst*I sites of pASK-IBA7plus to generate IBA-Fd (Table 1) with an N-terminal strep-tag fusion.

A 486-bp fragment containing the allophycocyanin α subunit (*apcA*) was PCR-amplified from *Synechocystis* genomic DNA using primers ApcA-F and ApcA-R (Additional file 1: Table S1). The PCR product was digested with *Bam*HI and *Pst*I, and ligated into the *Bam*HI/*Pst*I sites of pASK-IBA7plus to generate IBA-ApcA (Table 1) with an N-terminal strep-tag fusion.

A 489-bp fragment containing the phycocyanin α subunit (*cpcA*) was PCR-amplified from *Synechocystis* genomic DNA using primers CpcA-F and CpcA-R (Additional file 1: Table S1). The PCR product was digested with *Bam*HI and *Pst*I, and ligated into the *Bam*HI/*Pst*I sites of pASK-IBA7plus to generate IBA-CpcA (Table 1) with an N-terminal strep-tag fusion.

A 1.5-kb fragment containing water-forming NADH oxidase (Nox) (*noxV*) was PCR-amplified from *Lactobacillus plantarum* genomic DNA with the primers Nox-F/R (Additional file 1: Table S1). The PCR product was digested with *Bam*HI and *Pst*I, and ligated into the *Bam*HI/*Pst*I sites of pRSET-A to produce pRSET-Nox (Table 1) with an N-terminal his_6-tag fusion. The mutant enzyme NoxG178R was generated from pRSET-Nox with the primers Nox178-F and Nox178-R (Additional file 1: Table S1) using PrimeSTAR Max (Takara Bio, Japan). The resulting PCR product was treated with *Dpn*I to destroy the methylated parental DNA, followed by transformation into *E. coli*. Plasmid pRSET-Nox178 (Table 1), harboring the G178R mutation, was validated through sequencing. Accordingly, primers Nox178179-F and Nox178179-R (Additional file 1: Table S1) were used to construct pRSET-Nox178179 (Table 1) from pRSET-Nox178, as described above. It has G178R and L179R double-mutated sites, which were verified via sequencing.

A 1.5-kb fragment containing catalase (*katE*) was PCR-amplified from *Vibrio vulnificus* genomic DNA using primers KatE-F and KatE-R (Additional file 1: Table S1). The PCR product was digested with *Bam*HI and *Pst*I, and ligated into the *Bam*HI/*Pst*I sites of pASK-IBA3plus to generate IBA-KatE (Table 1) with a C-terminal strep-tag fusion.

Plasmid conjugation

Plasmids were mobilized from *E. coli* S17-1 to *Synechocystis* as previously described [35]. Exponential phase *E. coli* S17-1 harboring pSL-AtpB or pSL-AtpH and *Synechocystis* were mixed in a 1:1 ratio (v/v). The mating mixture was left on BG-11 medium containing 5% LB at 30°C for 12 h under white light (50 μmol m^{-2} s^{-1}). The exconjugants carrying pSL-AtpB or pSL-AtpH were selected on BG-11 medium containing Gm.

Purification of TM from *Synechocystis*

TMs were purified as previously described [7], with some modifications. Cells were harvested from 1 L of culture and suspended in TM buffer (10 mM sodium phosphate (pH 7.5), 5% sucrose, 10 mM $MgCl_2$, 5 mM sodium ascorbate, and 5% betaine) on ice, followed by disruption by sonication for 5 min for a total of three times. Ascorbate was added to the buffer to quench singlet oxygen. Cell debris was removed by centrifugation at 5000*g* for 10 min at 4°C. The resulting supernatant was subjected to ultracentrifugation at 150,000*g* and 4°C for 1 h to obtain the total cell membrane. It was suspended in 2 mL ice-cold TM buffer and loaded onto a discontinuous sucrose density gradient (60%, 40%, 20% (w/v)), followed by ultracentrifugation at 150,000*g* and 4°C for 3 h. The chlorophyll a (Chl *a*)-condensed layer between 40 and 20% sucrose was collected as the TM fraction, which was then diluted with an equal volume of 10 mM sodium phosphate buffer (pH 7.5) and kept at −80°C in the dark for further analysis.

Determination of Chl *a* content

The Chl *a* content of the TM was determined as previously described [38]. Briefly, 10 μL of purified TM was dissolved in 500 μL acetone/methanol (7/2, v/v) via a brief vortex. This was followed by centrifugation at 15,000*g* at 4°C for 1 min. The pigment content was determined with an extinction coefficient of $\varepsilon_{660} = 77.1$ mM^{-1} cm^{-1} [38].

Preparation of TMs harboring his_6-tagged β ($TM_{β\text{-}his}$) and strep-tagged c ($TM_{c\text{-}strep}$) subunits of ATP synthase

We determined whether ATP synthase enzymes of the TM vesicles are oriented outward or inward through previously described methodology [39], with some modifications. The his_6-tagged β subunit and strep-tagged c subunit were assembled into ATP synthase in the recombinant strains Syn-AtpB and Syn-AtpH (Table 1), respectively. $TM_{β\text{-}his}$ and $TM_{c\text{-}strep}$ were prepared and loaded onto columns containing Ni–NTA and streptavidin resins within a linear range of binding capacity. The flow-through fraction (FF) was interpreted to have TM vesicles containing the inside orientation of the tag, whereas the elution fractions

(EF) were interpreted to have an outside orientation of the tag. The FF and EF were adjusted to the same volume before separation via SDS-PAGE. The wash fraction (WF) was included as a control. Proteins were transferred to polyvinylidene difluoride (PVDF) membranes and probed with anti-his_6-tag antibody (D291-3, MBL) or anti-strep-tag antibody (2-1507-001, IBA Life Sciences). An HRP-conjugated anti-mouse antibody (#7076, Cell Signaling Technology) was used to visualize the signal, which was detected by reaction with an ECL working solution (iNtRON Biotechnology, Korea).

To determine the tagging % from the total contents of subunits β and c, the TMs were pretreated with 0.5% Triton X-100 prior to affinity chromatography. The following procedure was performed as described above. One of the duplicated protein blots was further examined with either an anti-β antibody (generated using immunogen of β subunit, see below) or anti-c antibody (AS05 071, Agrisera) to determine the extent to which the tagged subunit was incorporated into the ATP synthase of the TM. HRP-conjugated anti-rat antibody (sc-2006, Santa Cruz Biotechnology) and anti-rabbit antibody (#7074, Cell Signaling Technology) were used to probe the β- and c-subunits, respectively. The bands were visualized by reaction with ECL working solution, and all quantifications were processed using ImageJ.

Purification of PBS from *Synechocystis*

PBS was isolated from *Synechocystis* as previously described [40]. Cells were harvested and suspended in 0.8 M potassium phosphate buffer (pH 7.0) before breakage by sonication. Supernatant from the cell lysate was treated with 2% Triton X-100 at 20°C for 30 min and subjected to ultracentrifugation at 150,000*g* and 20°C for 20 min. The clear blue layer containing PBS was collected and loaded onto a sucrose density gradient (1 mL of 2.0 M, 3 mL of 1.0 M, 2.5 mL of 0.75 M, 2.5 mL of 0.5 M, 2 mL of 0.25 M sucrose in 0.8 M potassium phosphate buffer (pH 7.0)), followed by ultracentrifugation at 150,000*g* and 20℃ for 16 h. PBS was obtained at the layer between 1.0 M and 0.75 M sucrose. It was then stored at 4°C in the dark until further use. Phycocyanin and allophycocyanin concentrations were calculated using the following equations: [41]

$$\text{Phycocyanin} = (A_{615} - 0.474 * A_{652})/5.34 \left(\text{mg mL}^{-1}\right)$$

$$\text{Allophycocyanin} = (A_{652} - 0.208 * A_{615})/5.09 \left(\text{mg mL}^{-1}\right)$$

Purified PBS consisted of phycocyanin and allophycocyanin at a ratio of approximately 2:1 (w/w).

EDTA treatment of TM

The F_1 complex of ATP synthase was removed from the TM with EDTA, as previously described [42, 43], with some modifications. TM containing 20 μg Chl *a* mL^{-1} was mixed with varying concentrations of EDTA in Mg-free TM buffer (10 mM sodium phosphate (pH 7.5), 5% sucrose, 5 mM sodium ascorbate, and 5% betaine) and incubated at 4°C for 1 h. The mixture was then subjected to sonication on ice, six times for 30 s each (with a 50% duty cycle). The EDTA-treated TM (TMe) was washed twice with TM buffer by ultracentrifugation at 150,000*g* and 4°C for 1 h. TMe was kept at 4°C in the dark until use.

Reconstitution of TM with PBS

TM (or TMe) containing 5 μg Chl *a* mL^{-1} was mixed with varying levels of PBS (One equivalent of PBS consists of phycocyanin (3.6 μg mL^{-1}) and allophycocyanin (1.8 μg mL^{-1})) in a total volume (4 mL) of TM buffer, followed by incubation at room temperature for 20 min in dark. Free PBS was removed by ultracentrifugation at 150,000*g* and 4°C for 1 h. The resulting PBS-reconstituted TM (pTM) (or PBS-reconstituted TMe (pTMe)) was kept at 4°C in the dark until use.

Determination of ATP and NADPH generation activity of TMs

ATP and NADPH generation activities were measured using TM (or pTM) at 5 μg Chl *a* mL^{-1} in TM buffer supplemented with 1 μM FNR, 10 μM Fd, 2 mM $NADP^+$, and 2 mM ADP (TM-$NADP^+$-ADP buffer). When TM was deprived of the F_1 complex of ATP synthase with EDTA, NADPH generation activity was determined using TM buffer supplemented with 1 μM FNR, 10 μM Fd, and 2 mM $NADP^+$ (TM-$NADP^+$ buffer). The reaction mixture was incubated at 30°C under white light (50 μmol m^{-2} s^{-1}). The reaction in the dark was used as a control. Aliquots of samples were taken at 30-min intervals and stored at −80°C prior to analysis. NADPH was detected based on changes in the absorbance at 340 nm over a time-course and calculated with an extinction coefficient of 6.22 mM^{-1} cm^{-1}, whereas ATP was determined using an ATP Colorimetric/Fluorometric Assay Kit (K354, BioVision). All quantifications were independently repeated three times, and data are shown as the mean ± standard deviation (SD).

Treatment of pTM with carbonyl cyanide-p-(trifluoromethoxy) phenylhydrazone (FCCP)

pTM containing 5 μg Chl *a* mL^{-1} was added to TM-$NADP^+$-ADP buffer supplemented with varying levels (0–10 μM) of FCCP. The mixtures were incubated at

room temperature for 20 min in the dark, followed by the measurement of ATP and NADPH generation, as described above.

Preparation or acquisition of antiserums for western blot analysis

Each subunit (α, β, γ, δ, and ε) of ATP synthase as well as each α subunit of allophycocyanin and phycocyanin in PBS was expressed in *E. coli* BL21(DE3) and purified for use as immunogens to prepare rat antiserum as previously described [44]. The resulting antisera were used to probe the target bands at a dilution of 1:2000 for western blot analysis, as previously described [45].

Antibodies PsbO (AS06 142–33), PsbA (AS10 703), PC (AS06 141), and PsaC (AS10 939) were purchased from Agrisera (Sweden) and used according to the manufacturer's instructions in order to examine the stability of TM photosynthetic machinery. The target bands that reacted with the above antibodies were incubated with an HRP-conjugated anti-rat antibody (sc-2006, Santa Cruz Biotechnology) or an anti-rabbit antibody (#7074, Cell Signaling Technology) to develop signals using ECL working solution, followed by quantification with ImageJ.

Biosilicification of pTMe

pTMe was biosilicified as previously described [46]. pTMe containing 10 μg Chl *a* mL^{-1} was mixed with R5 (synthesized by Anygen, Korea) at 0.5 mg mL^{-1} in TM buffer and incubated at room temperature for 5 min. Silicic acid was prepared as previously described [46]. Briefly, tetramethyl orthosilicate (TMOS) at 1 M was prehydrolyzed at room temperature for 30 min in 1 mM hydrochloric acid. TMOS was added at a concentration of 10 mM to pTMe pretreated with R5, and biosilicification proceeded by incubating the mixture at room temperature for 30 min. The resulting biosilicified pTMe (b-pTMe) was washed three times with TM buffer via centrifugation at 3000*g* at 4°C. The resulting pellet was suspended in TM buffer and stored at 4°C in the dark until further use.

Examination of zeta potential

pTMe, pTMe pre-incubated with R5 as described above, and b-pTMe were prepared at 5 μg Chl *a* mL^{-1} for the measurement of zeta potential with a Zetasizer Nano S (Malvern, UK). pTMe pre-incubated with R5 was washed twice with TM buffer via ultracentrifugation at 150,000*g* and 4°C for 30 min to remove any free R5. All quantifications were independently repeated three times, and data are shown as the mean ± standard deviation (SD).

Determination of pTMe and b-pTMe sustainability

pTMe and b-pTMe were prepared at 5 μg Chl *a* mL^{-1} in 10 mL of TM-$NADP^+$ buffer (10 mL). Reaction mixtures were incubated at 30°C in the dark for one week or in white light (50 μmol m^{-2} s^{-1}) for two days. Aliquots (0.5 mL) were withdrawn intermittently from each sample and washed with TM buffer three times via ultracentrifugation at 150,000*g* and 4°C for 30 min prior to the activity assays. NADPH production was determined in TM-$NADP^+$ buffer at 30°C under white light (50 μmol m^{-2} s^{-1}).

Examination of R5 antioxidant activity

Singlet oxygen generation and quenching were examined as previously described [47]. To determine the antioxidant activity of R5 peptide, varying levels of R5 were prepared in 0.1 mM phosphate buffer (pH 7.0), followed by the addition of linoleic acid in ethanol to a final concentration of 50 mM. Histidine (3 mM) was used as a positive control. The reaction mixtures were placed under white light (50 μmol m^{-2} s^{-1}) after the addition of 0.1 mM methylene blue. Samples were withdrawn at 1-h intervals. The peroxide content was measured via the ferric thiocyanate method [48]. Ferric thiocyanate complex was detected at 500 nm. Quenching of singlet oxygen was calculated as inhibition % using the following equation: Inhibition (%) = $(A_0–A_1)/A_0 \times 100$, where A_0 is the absorption of the control after 1-h irradiation, and A_1 is the absorption of samples containing R5 or histidine after the same period of irradiation.

The superoxide scavenging activity of R5 was measured using xanthine and xanthine oxidase (Roche) in the presence of nitroblue tetrazolium chloride (NBT) [49]. Xanthine is oxidized by xanthine oxidase to generate superoxide, which can oxidize NBT to formazan, as indicated by the absorbance at 560 nm. The reaction mixture (1 mL) consisted of varying concentrations of R5, 0.2 mM xanthine, 0.5 U mL^{-1} xanthine oxidase, and 0.5 mM NBT. Bovine superoxide dismutase (SOD) (5 U mL^{-1}) (Sigma S9697) was used as the positive control. The reaction was performed at room temperature for 20 min, and the scavenging activity of superoxide was calculated as inhibition % using the following equation: Inhibition (%) = $(A_0–A_1)/A_0 \times 100$, where A_0 is the absorption of the control after a 20-min reaction, and A_1 is the absorption of samples containing R5 or bovine SOD after reaction for the same period.

Hydrogen peroxide (H_2O_2) scavenging assays were performed as described previously [50]. The reaction mixture (0.5 mL) consisted of varying concentrations of R5 and 100 mM H_2O_2 in 10 mM phosphate buffer (pH 7.5). Catalase (30 μg mL^{-1}) was used as the positive control.

After reaction at 30°C for 5 min, the absorption at 230 nm was monitored. The scavenging activity of hydrogen peroxide was calculated as inhibition % using the following equation: Inhibition (%) = $(A_0–A_1)/A_0 \times 100$, where A_0 is the absorption of the samples at time zero, and A_1 is the absorption of the sample after reaction for 5 min.

Purification of water-forming NADPH oxidase and determination of its activity

Water-forming NADPH oxidase (Nox^m) was produced from *E. coli* BL21(DE3) harboring pRSET-Nox178179 (Table 1) and purified using Ni–NTA resin as previously described [51]. The NADPH oxidation activity of Nox^m was determined as previously described [34]. The reaction mixture (0.5 mL) consisted of varying concentrations of NADPH (0–100 µM) in 10 mM phosphate buffer (pH 7.5). The assay was conducted at 30°C, and NADPH was determined at 340 nm with an extinction coefficient of 6.22 mM^{-1} cm^{-1}.

Detection of ROS generated by pTMe and b-pTMe

The singlet oxygen generated by pTMe and b-pTMe in light was determined using Singlet Oxygen Sensor Green (SOSG) (Invitrogen™, S36002), as previously described [52, 53]. SOSG was prepared at 50 µM in TM-$NADP^+$ buffer (0.2 mL) containing either pTMe or b-pTMe (5 µg Chl *a* mL^{-1}). The mixture was added into a black 96-well microtiter plate covered with a transparent lid. After incubation at 30°C for 30 min under 50 µmol m^{-2} s^{-1} white light, fluorescence was detected at 525 nm with excitation at 504 nm. Measurements were performed within a linear relationship between the levels of pTMe (or b-pTMe) and the fluorescence signal at 525 nm. Fluorescence from SOSG without pTMe or b-pTMe addition was used as a negative control. All quantifications were independently repeated three times, and data are shown as the mean ± standard deviation (SD).

General ROS generated by pTMe and b-pTMe in light, including hydrogen peroxide, hydroxyl radicals, peroxyl radicals, and peroxynitrite, were detected with H_2DCFDA (Sigma-Aldrich). Either pTMe or b-pTMe (each at 5 µg Chl *a* mL^{-1}) was mixed with TM-$NADP^+$ buffer and incubated at 30°C for 2 h under 50 µmol m^{-2} s^{-1} white light. Aliquots (0.2 mL) were withdrawn and lysed with 4 µL chloroform, followed by vigorous vortexing. The samples were transferred to a black 96-well microtiter plate containing H_2DCFDA (0.1 mM) and the cell lysate (32 µg) of *Synechocystis* as an esterase source to detect general ROS after incubation at 30°C in the dark for 10 min. Fluorescence at 525 nm was detected within a linear relationship with the level of pTMe (or b-pTMe) after excitation at 488 nm. The reaction without pTMe or b-pTMe was used as a negative control. All quantifications were independently repeated three times, and data are shown as the mean ± standard deviation (SD).

Results and discussion

Examination of structure of the purified TM

Two different types of vesicles can be obtained when TMs are prepared via sonication cell lysis: ATP synthase F_1-out and F_1-in orientation [54, 55]. An F_1-out vesicle is the structure that can generate NADPH and ATP using light. To evaluate the proportion of F_1-out vesicles, the β (F_1)-and c (F_o)-subunits of ATP synthase were analyzed for membrane orientation. Previously, the his_6-tagged β-subunit was introduced into the ATP synthase of artificial proteoliposomes, and the membrane orientation was determined by inspecting its binding to Ni–NTA magnetic beads [39].

The recombinant β-subunit with a his_6-tag at its N-terminus was produced in Syn-AtpB (Table 1), and TM was obtained from cells via sucrose density gradient ultracentrifugation. In order to detect F_1-out vesicles, varying amounts of TM, which were determined with Chl *a* unless stated otherwise, were loaded onto the Ni–NTA column within the binding capacity of the resin for the tag, as previously described [14]. Unbound free TM was removed by washing, and the Chl *a* content of resin-bound $TM_{β\text{-}his}$ was determined after acetone/methanol extraction. The maximum binding capacity was approximately 3.4 µg Chl *a* per mL Ni–NTA resin (Additional file 1: Fig. S1A).

TM in the elution fraction (EF) was regarded as an F_1-out vesicle with his_6-tagged β, whereas TM in the flow-through fraction (FF) was regarded as an F_1-in vesicle (Fig. 1A, left). Western blot analysis with the his_6 antibody revealed approximately 74% of the signal from EF, suggesting that F_1-out vesicles accounted for the majority of $TM_{β\text{-}his}$. His_6-tag-free vesicles with an F_1-out orientation could be included in FF (Fig. 1A, left), although not detected. Accordingly, the amount of his_6-tagged β-subunit incorporated into the ATP synthase of TM was determined. To this end, the TM was treated with Triton X-100 (0.5%) to expose the total β subunits prior to loading onto the Ni–NTA column. Most (96%) his_6-tagged β-subunits were detected in the EF (Fig. 1A, middle). The minor (4%) signal from FF could be ascribed to the tagged subunit overflow because Ni–NTA resin was used at the maximum binding capacity. The same samples were analyzed via western blot using an anti-β antibody. Approximately the same signal intensities were detected in both FF and EF (Fig. 1A, right), suggesting that half of the β-subunits in F_1-ATPase of TMs were his_6-tagged.

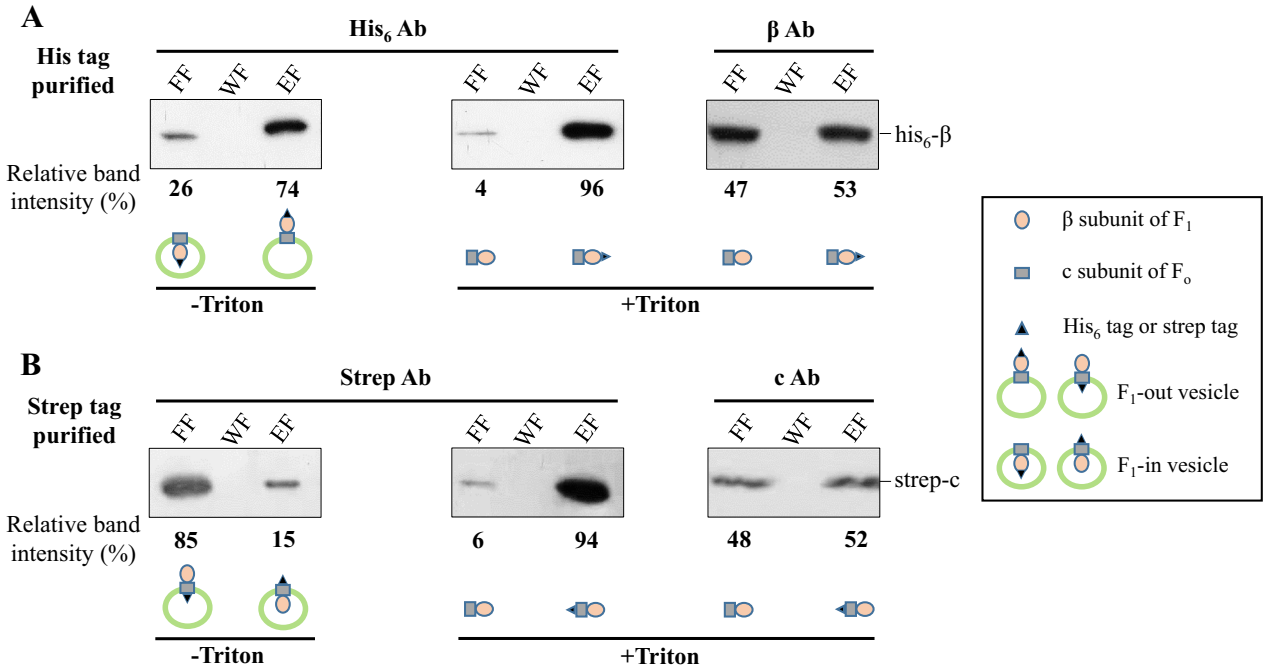

Fig. 1 Structure of the purified TM. **A** TM prepared from Syn-AtpB contains the his_6-tagged β subunit (52.7 kDa) of ATP synthase ($TM_{β\text{-}his}$), which was subjected to Ni–NTA affinity purification within a linear range of binding capacity. Fractions of FF, WF, and EF were separated via SDS-PAGE and evaluated for presence of the his_6-tagged β subunit via western blot with the his_6 antibody (left). In order to determine the proportion of the his_6-tagged β subunit in ATP synthase, $TM_{β\text{-}his}$ was pretreated with 0.5% Triton X-100 prior to loading onto Ni–NTA resin. FF, WF, and EF were separated via SDS-PAGE and evaluated for his_6-tag and β subunit by western blot with antibodies against the his_6 and β subunit, respectively (middle and right). **B** TM prepared from Syn-AtpH contains the strep-tagged c subunit (8.8 kDa) of ATPase ($TM_{c\text{-}strep}$), which was subjected to streptavidin-based affinity purification within linear range of binding capacity. Fractions of FF, WF, and EF were separated via SDS-PAGE and evaluated for the strep-tagged c-subunit via western blot with the anti-c antibody (left). In order to determine the proportion of strep-tagged c-subunit in ATP synthase, $TM_{c\text{-}strep}$ was pretreated with 0.5% Triton X-100 prior to loading onto streptavidin resin. FF, WF, and EF were separated via SDS-PAGE and evaluated for the streptavidin tag and c-subunit through western blot with antibodies against streptavidin and the c-subunit, respectively (middle and right)

To confirm these results, the N-terminus of the c-subunit of F_o, which is exposed at the site opposite to the β subunit, was tagged with streptavidin. The recombinant strep-tagged c subunit was produced in Syn-AtpH (Table 1), and TM was prepared from the cells. The binding capacity of streptavidin resin for TM containing the strep-tagged c subunit exposed outside was determined as described above, which turned out to be around 1.2 μg Chl *a* per mL resin (Additional file 1: Fig. S1B).

The TM in FF was regarded as an F_o-in vesicle, whereas the TM in EF was regarded as an F_o-out vesicle with strep-tagged c (Fig. 1B, left). Western blotting with an anti-strep antibody revealed approximately 85% signal from FF, suggesting F_1-out (F_o-in) vesicles as the major portion of $TM_{c\text{-}strep}$. This result also confirmed the above results obtained with the his_6 tag, and more than three-quarters of TMs prepared from *Synechocystis* were in the orientation of F_1-out (F_o-in). Strep-tag-free vesicles were included in FF (Fig. 1B, left), although they were not detected. Accordingly, the extent of incorporation of the strep-tagged c-subunit into the ATP synthase of TM was determined. The TM was treated with Triton X-100 (0.5%) to expose the total c subunits prior to loading onto the streptavidin column. Most (94%) strep-tagged c-subunits were detected in the EF (Fig. 1B, middle). The minor (6%) signal from FF could also be ascribed to the tagged subunit overflow because streptavidin resin was used at the maximum binding capacity. The same samples were analyzed by western blotting using an anti-c antibody. Similarly, approximately the same signal intensities were detected in both FF and EF (Fig. 1B, right), suggesting that half of the c-subunits in the F_o-ATPase of TM were strep-tagged.

Enhancement of NADPH generation by removal of the F_1 complex from ATP synthase

TM components can support the light-dependent generation of NADPH and ATP when $NADP^+$ and ADP are present along with Fd and FNR [11, 13]. As anticipated, light-dependent generation of NADPH and ATP

was observed with the purified TM (Additional file 1: Fig. S2). Fd and FNR were optimized to further enhance TM activity (Additional file 1: Fig. S3). The NADPH generation rate increased with the Fd concentration, but a higher amount of Fd (≥ 20 μM) inhibited this activity (Additional file 1: Fig. S3A). This result was in line with previous studies [13, 56], which showed that higher levels of Fd may lead to the accumulation of complexes between oxidized Fd and FNR-containing semiquinone FAD. An increase in FNR (1–2 μM) slightly enhanced activity (Additional file 1: Fig. S3B), implying that FNR is primarily associated with the purified TM. The PBS is a light-harvesting antenna that is easily lost during TM preparation (Additional file 1: Fig. S4 Lanes 1 and 2). To compensate for this loss, PBS was isolated and used for reconstitution of the purified TM. NADPH generation increased in a dose-dependent manner when reconstituted with up to 5 equivalents (EQs) of PBS (Additional file 1: Fig. S3C). One EQ of PBS was arbitrarily set as phycocyanin at 3.6 μg mL^{-1} and allophycocyanin at 1.8 μg mL^{-1} because purified PBS consists of phycocyanin and allophycocyanin at a ratio of approximately 2:1 (w/w). Western blot analysis demonstrated that PBS content was recovered up to 80–90% via reconstitution (Additional file 1: Fig. S4, lane 5). The rate of light-dependent NADPH generation by TM reconstituted with 5 EQs of PBS was approximately 45 nmol min^{-1} Chl *a* mg^{-1} (Fig. 2A) in the presence of 1 μM FNR and 10 μM Fd.

A previous study demonstrated that a high proton gradient of the TM inhibited the LEF [57]. Moreover, excess protons cause luminal acidification, which can downregulate photosynthetic electron transport [58]. Given the coupling of LEF with proton movement, disruption of this linkage would relieve the inhibitory effect of ΔpH on LEF. The protonophore FCCP was used to dissipate pmf [59]. As expected, the NADPH generation rate increased approximately two-fold in a dose-dependent manner when pTM (TM reconstituted with 5 EQs of PBS) was treated with up to 5 μM FCCP (Fig. 2B). A concomitant decline in ATP generation was observed (Additional file 1: Fig. S5). However, FCCP treatment may also trigger ROS generation [60, 61]. Therefore, other approaches to achieve this goal must be developed.

It was previously shown that cleavage of the F_1 γ subunit of ATP synthase can lower the proton gradient by inducing proton leakage [62, 63]. Therefore, the F_1 complex of ATP synthase was removed using EDTA. EDTA-sonic treatment was applied to the deprivation of F_1 subunits [42]. An increase in the NADPH generation rate of approximately 35% was observed after treatment with 2.5 mM EDTA (Additional file 1: Fig. S6A). The residual subunits were examined via western blot analysis using antibodies against each subunit. The results revealed that F_1 was deprived of approximately half of γ by increasing EDTA up to 10 mM, while more than 90% of the other subunits were removed (Additional file 1: Fig. S6B). As anticipated, ATP generation decreased after the same treatment (Additional file 1: Fig. S6C). No further enhancement of NADPH generation was observed at EDTA higher than 2.5 mM (Additional file 1: Fig. S6A).

Given the labile charge-charge interactions between PBS and TM [64], higher concentrations of EDTA could also remove PBS, as previously reported [65]. In fact,

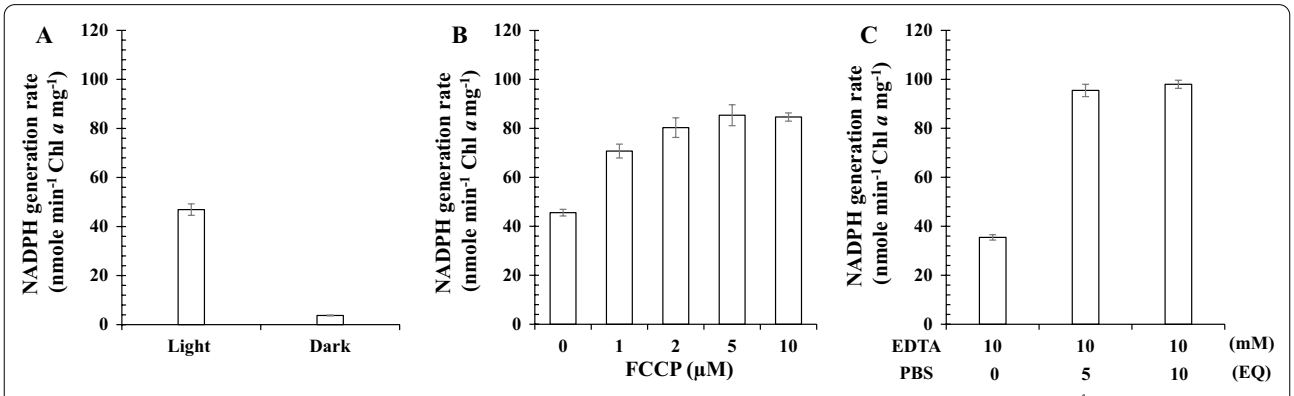

Fig. 2 NADPH generation by pTM in the presence of FCCP and by the PBS-reconstituted TMe (pTMe). **A** pTM (5 μg Chl *a* mL^{-1}) was mixed with TM-$NADP^+$ buffer. The NADPH generation rate was determined under white light (50 μmol m^{-2} s^{-1}) and in the dark. **B** The NADPH generation of pTM (5 μg Chl *a* mL^{-1}) was measured in the presence of varying concentrations of FCCP (0–10 μM) under white light as described in (**A**). **C** TM (5 μg Chl *a* mL^{-1}) was treated with 10 mM EDTA as described in the Materials and Methods. The resulting TMe was washed with TM buffer via ultracentrifugation at 150,000*g* and 4℃ for 1 h, followed by reconstitution for PBS with 5 and 10 EQs. The resulting pTMe was examined for NADPH generation as described in (**A**). One EQ of PBS consists of 3.6 μg mL^{-1} phycocyanin and 1.8 μg mL^{-1} allophycocyanin. All quantifications were independently repeated three times, and data are shown as the mean ± standard deviation (SD)

PBS of the EDTA (10 mM)-treated TM (TMe) was barely detected via western blot analysis using antibodies against the α subunits of allophycocyanin and phycocyanin (Additional file 1: Fig. S7 lane 1). Therefore, TMe was reconstituted with 5 and 10 EQs of PBS to yield pTMe, revealing an approximately five- to ten-fold increase in PBS content (Additional file 1: Fig. S7). The NADPH generation activity of pTMe reconstituted with 5 EQs was similar to that of pTMe with 10 EQs (Fig. 2C), which is approximately twice as large as that of TMe (10 mM EDTA without PBS reconstitution). Therefore, pTMe reconstituted with five EQs was used in subsequent experiments.

Sustainability improvement via biosilicification

To protect the lipid bilayer and protein-pigment complexes of TM from external stress, they were kept in a defined space via coating with a rigid silica shield. Silaffin-derived peptide R5 (SSKKSGSYSGSKGSKRRIL) has been shown to mediate silicification, which can encapsulate proteins and bacteria to enhance stability and survivability [26, 46]. Inspired by this process, pTMe was biosilicified using R5 with a TMOS (Additional file 1: Fig. S8A and B). Biosilicified pTMe (b-pTMe) was fully precipitated via centrifugation even at 3000*g* for 1 min. Examination of NADPH generation activity of pTMe revealed that R5 and TMOS did not have any deleterious effects on NADPH generation (Additional file 1: Fig. S8A and B, white bars). pTMe could be biosilicified up to 40 μg Chl *a* mL^{-1} using R5 (0.5 mg mL^{-1}) with TMOS (10 mM) (Additional file 1: Fig. S8C).

The fluorescence microscopy image of b-pTMe demonstrated an amorphous structure with a diameter in the range of 3 to 6 μm (Additional file 1: Fig. S9B), which was much larger than that of pTMe (Additional file 1: Fig. S9A). The Z-average of pTMe is approximately 160 nm (Additional file 1: Fig. S9C). As basic R5 is absorbed by pTMe, the surface charge increases in the positive direction. However, this was lowered back to the negative side when encapsulated with a silica shell by R5 (Additional file 1: Fig. S10), demonstrating surface changes caused by biosilicification.

We investigated whether the sustainability of pTMe was improved by biosilicification. pTMe and b-pTMe were placed in TM-$NADP^+$ buffer at 30°C in the presence or absence of light, respectively. Approximately 80% of the NADPH generation activity of b-pTMe was preserved even after seven days in the dark, whereas only 30% activity was observed with pTMe under the same conditions (Fig. 3A). Thus, biosilicification improved the sustainability of NADPH generation. To investigate the matter further, levels of the four major components of LEF, PsbO (subunit of water splitting complex), PsbA (photosystem II protein D1), PC (luminal electron carrier), and PsaC (stromal subunit of photosystem I), were examined via western blot analysis. The four pTMe proteins exhibited decreases between days 3 and 7 (Additional file 1:

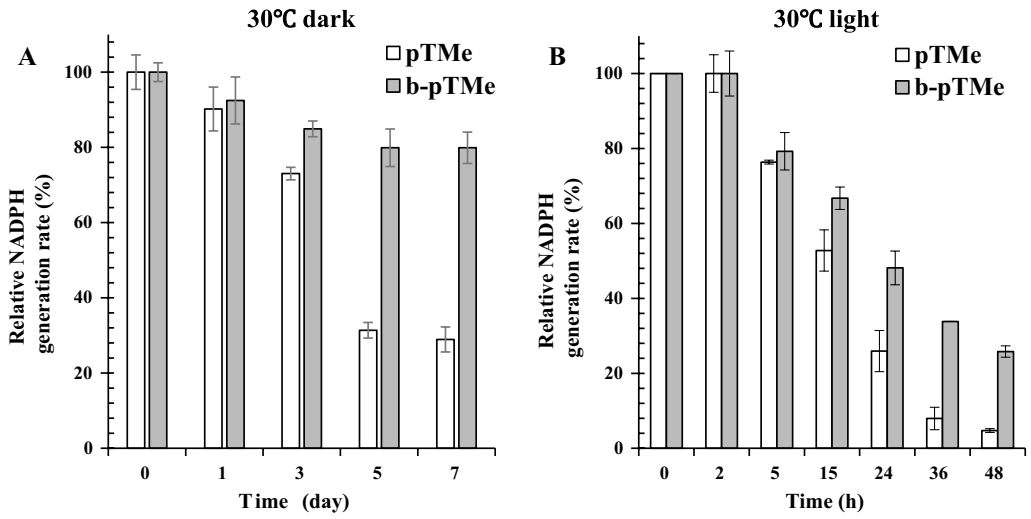

Fig. 3 Sustainability of NADPH generation by pTMe and b-pTMe. pTMe and b-pTMe were kept in TM-$NADP^+$ buffer at 30℃ for one week in dark (**A**) or for 48 h under white light (50 μmol m^{-2} s^{-1}) **B**. Aliquots were withdrawn at time points indicated and briefly washed via ultracentrifugation (150,000*g* and 4℃ for 30 min). NADPH generation by pTMe and b-pTMe (each at 5 μg Chl *a* mL^{-1}) were evaluated in TM-$NADP^+$ buffer at 30℃ under white light (50 μmol m^{-2} s^{-1}). The relative activities of pTMe and b-pTMe were represented as percentages of TM activity at time zero, which were virtually the same. All measurements were independently repeated three times, and data are shown as the mean ± standard deviation (SD)

Fig. S11A). Conversely, no less than 40% of each protein remained in b-pTMe for 7 days (Additional file 1: Fig. S11B). These results demonstrated the protective effect of the silica shell on NADPH generation.

NADPH generation activities of pTMe and b-pTMe in light decreased more drastically in two days compared with those in the dark (Fig. 3B), although biosilicification still exhibited a positive effect on NADPH generation. The four proteins involved in LEF were examined by western blotting, as described above. The results showed that fewer proteins remained after two days (Additional file 1: Fig. S12) compared to those after 3-day storage in the dark (Additional file 1: Fig. S11). This may be ascribed to the ROS generated under light, which can damage membrane lipids and protein [29], especially PsbA and PsbD in photosystem II [66].

General ROS formation by pTMe and b-pTMe in light was examined using the ROS indicator H_2DCFDA. The cell lysate (32 μg) from *Synechocystis* was used as an esterase source to hydrolyze H_2DCFDA (Additional file 1: Fig. S13A and B), and chloroform (4 μL) was used to lyse pTMe and b-pTMe in order to detect ROS formed inside the vesicle (Additional file 1: Fig. S13C and D). Singlet oxygen generated by pTMe and b-pTMe in light was also determined using SOSG. The singlet oxygen content was reduced by approximately 30% via biosilicification (Additional file 1: Fig. S14A), whereas general ROS formation was unaffected (Additional file 1: Fig. S14B). The -Si-O-Si- bond in silica [67] was found to be nonresponsive to ROS [68, 69]. Lysine (K) and arginine (R) were known to inhibit the oxidation of lipids and proteins by ROS [70, 71]. R5 (19 residues) contains four Ks and two Rs, which may possess antioxidative properties. Interestingly, R5 could quench singlet oxygen but did not scavenge superoxide or hydrogen peroxide (Additional file 1: Fig. S15). These results may account for the difference in singlet oxygen generation between pTMe and b-pTMe (Additional file 1: Fig. S14).

Decrease in singlet oxygen generation through sustained LEF activity with Nox^m

If NADPH is not oxidized instantly after its generation, electron flow in the TM (Fig. 4A) ceases with electron carriers in more reduced states. Accumulation of NADPH can induce over-reduction of plastoquinone [30], which may have detrimental effects on the photosystem through the formation of ROS [30, 31]. To keep electron carriers in a less reduced state, cyclic conversion between NADPH and $NADP^+$ was provided with an engineered water-forming NADPH oxidase (Nox^m) (Fig. 4B), which was derived from the Nox of *Lactobacillus plantarum* after introducing mutations

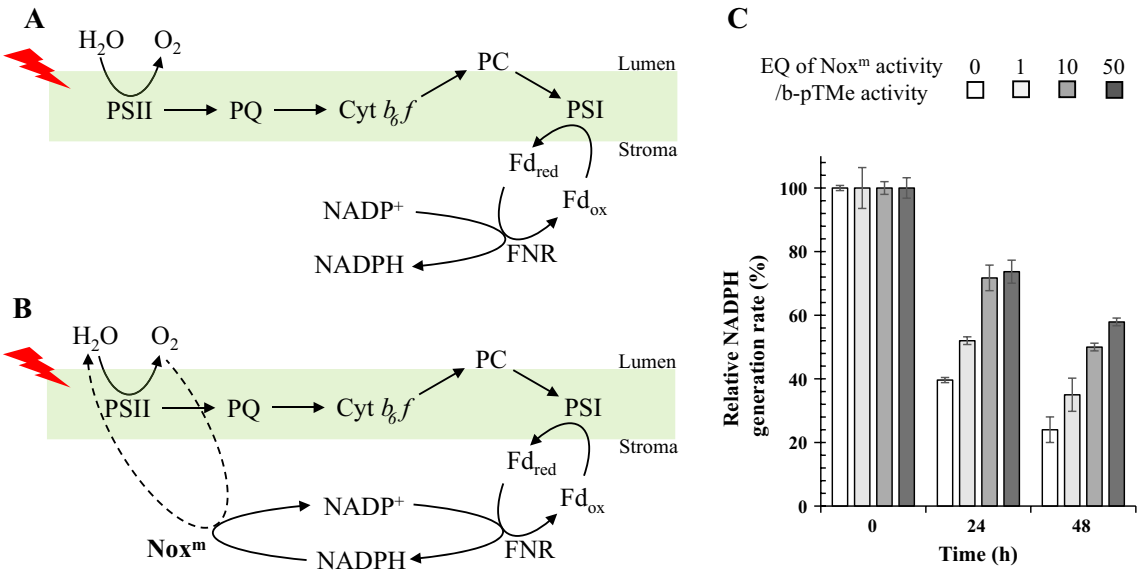

Fig. 4 Effect of Nox^m on the sustainability of b-pTMe at 30℃ under light. **A** The LEF of TM is illustrated with its main components. **B** NADPH is oxidized to $NADP^+$ by Nox^m with the simultaneous reduction of O_2 to H_2O. Thus, the cyclic conversion between $NADP^+$ and NADPH was provided to keep LEF running. **C** Nox^m was added to b-pTMe at EQ ratios of 1:1, 10:1, and 50:1 in TM-$NADP^+$ buffer, followed by incubation at 30℃ under white light (50 μmol m^{-2} s^{-1}). b-pTMe without Nox^m was included as control. Aliquots were withdrawn at time points indicated and washed three times via centrifugation (at 3000*g* and 4℃ for 3 min). NADPH generation by b-pTMe (5 μg Chl *a* mL^{-1}) was evaluated in TM-$NADP^+$ buffer at 30℃ under white light (50 μmol m^{-2} s^{-1}). The relative activities of b-pTMe were presented as percentages of those at time zero, which were virtually the same. All quantifications were independently repeated three times, and data are shown as the mean ± standard deviation (SD)

in G178R and L179R to obtain the substrate (i.e., coenzyme) preference for NADPH over NADH [34]. Nox^m was kinetically analyzed to illustrate activity of 18.1 ± 0.9 μmole min^{-1} mg^{-1} (Additional file 1: Fig. S16). The NADPH generation activity of pTMe (5 μg Chl *a* mL^{-1}) was approximately 100 nmol min^{-1} Chl *a* mg^{-1} (Fig. 2C), which was not affected by biosilicification (Additional file 1: Fig. S8). Varying levels of Nox^m were mixed with the b-pTMe reaction mixture in the light for two days (Fig. 4C). b-pTMe without Nox^m was included as a control. The amount of Nox^m that could oxidize NADPH formed by b-pTMe was approximately 28 ng, which was arbitrarily set as 1 EQ. Aliquots were withdrawn at the indicated time points and washed via centrifugation to remove the Nox^m. The absence of Nox^m after washing was confirmed through western blot with the anti-his_6-tag antibody (data not shown). The introduction of Nox^m substantially improved the sustainability of NADPH generation in a ratio-dependent manner (Fig. 4C), which correlated with a decrease in singlet oxygen generation (Fig. 5A). Thus, retaining LEF activity under light results in the alleviation of the single oxygen generation of TM, which may be ascribed to the maintenance of electron carriers in a less reduced state with decreased exciton pressure at the reaction center of PS II [31]. However, Nox^m had no obvious effect on general ROS formation (Fig. 5B).

Decrease in general ROS levels with catalase

We examined whether the antioxidant enzymes SOD and catalase reduced the general ROS formed by b-pTMe. SOD did not exhibit any effect, but catalase lowered the general ROS to half the levels observed in the control (Additional file 1: Fig. S17). Once superoxide is formed by TM, it can be rapidly reduced to H_2O_2. It has been proposed that plastohydroquinone of the chloroplast TM can scavenge superoxide radicals to form H_2O_2 [72]. Catalase activity was used to examine the sustainability of b-pTMe in the presence of Nox^m. General ROS levels were reduced to less than half through the addition of catalase (Fig. 6B), whereas singlet oxygen content was not affected (Fig. 6A). Consequently, approximately 80% of the NADPH production activity of b-pTMe was sustained in light for 48 h when catalase was added to the reaction mixture containing Nox^m (Fig. 7). Taken together, maintaining the NADPH utilization at no less than its formation and removing the hydrogen peroxide formed improved in vitro TM sustainability.

Practically, TM can be used for in vitro biosynthetic reactions requiring NADPH. If transhydrogenase [73] is

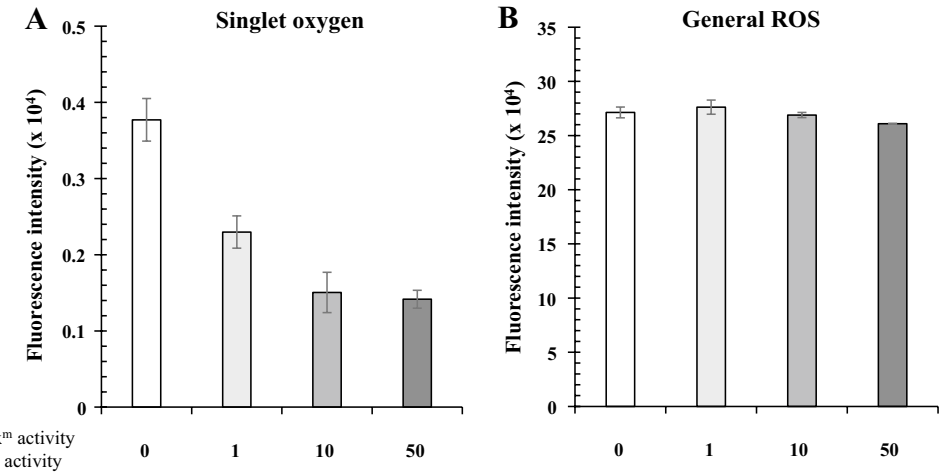

Fig. 5 Effect of Nox^m on ROS generation of b-pTMe at 30℃ under light. **A** In order to detect singlet oxygen generated by b-pTMe, Singlet Oxygen Sensor Green (SOSG, 50 μM) was added to the reaction mixture, which contained b-pTMe at 5 μg Chl *a* mL^{-1} in TM-$NADP^+$ buffer supplemented with varying EQ ratios of Nox^m. Reaction without Nox^m was included as a control. The reaction was performed at 30℃ for 30 min under 50 μmol m^{-2} s^{-1} white light. Fluorescence from SOSG was detected at 525 nm with excitation at 504 nm after 30 min irradiation. **B** General ROS was detected with 0.2 mL aliquot withdrawn from reaction mixture of pTMe and b-pTMe at 5 μg Chl *a* mL^{-1} in TM-$NADP^+$ buffer, which had been incubated at 30°C for 2 h under white light (50 μmol m^{-2} s^{-1}). pTMe and b-pTMe were lysed with 4 μL chloroform, and 0.1 mM H_2DCFDA was added to the reaction mixture with 32 μg *Synechocystis* cell lysate. The mixture was then incubated at 30°C for 10 min in dark, followed by detection of fluorescence at 525 nm after excitation at 488 nm. H_2DCFDA without Nox^m was included as a control. All the quantifications were independently repeated three times, and data are shown as the mean ± standard deviation (SD)

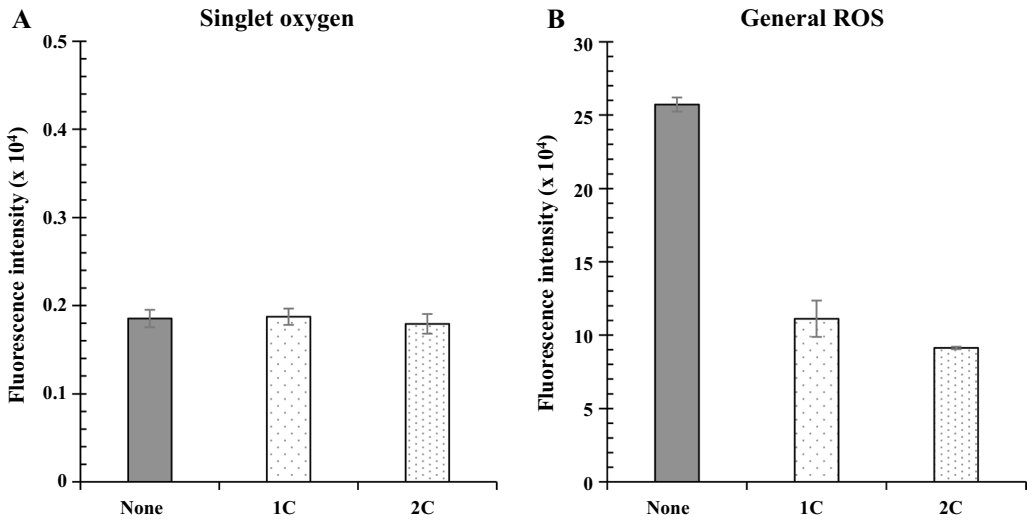

Fig. 6 Effect of catalase on ROS generation by b-pTMe in the presence of Nox^m. ROS generation was examined with b-pTMe (5 µg Chl *a* mL^{-1}) in TM-$NADP^+$ buffer supplemented with Nox^m (50 EQ ratios) and varying levels of catalase (1C, 37.5 µg mL^{-1}; 2C, 75 µg mL^{-1}). No addition of catalase (none) was included as a control condition. Singlet oxygen (**A**) and general ROS (**B**) were detected as described in Fig. 5. All quantifications were independently repeated three times, and data are shown as the mean ± standard deviation (SD)

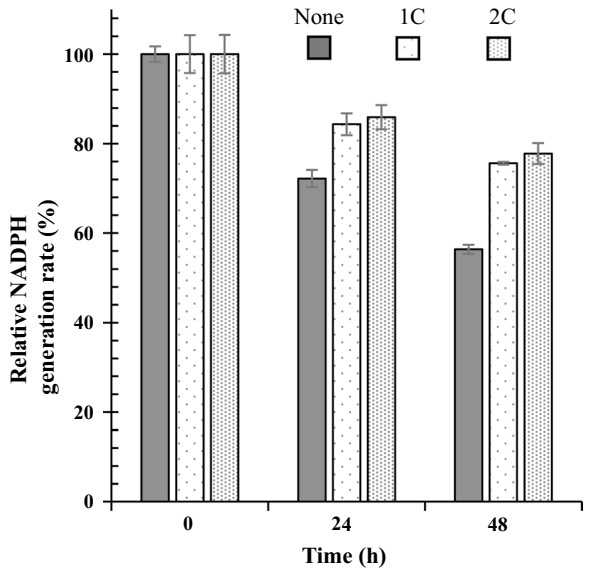

Fig. 7 Sustainability of NADPH generation from b-pTMe in the presence of Nox^m and catalase. NADPH generation was examined with b-pTMe (5 µg Chl *a* mL^{-1}) in TM-$NADP^+$ buffer supplemented with Nox^m (50 EQ ratios) and varying levels of catalase (1C, 37.5 µg mL^{-1}; 2C, 75 µg mL^{-1}). The reaction mixture was incubated at 30℃ for 48 h under white light (50 µmol m^{-2} s^{-1}). Aliquots were withdrawn at the indicated time points and washed three times via centrifugation (at 3000*g* and 4℃ for 3 min). NADPH generation by b-pTMe was evaluated in TM-$NADP^+$ buffer at 30℃ under white light (50 µmol m^{-2} s^{-1}). The relative activities of b-pTMe were represented as a percentage of those at time zero, which were virtually the same. All quantifications were independently repeated three times, and data are shown as the mean ± standard deviation (SD)

provided, NADH can be readily produced from NADPH. Moreover, the total yield of a target material from the biosynthetic pathway may be elevated by increasing the amount of TM in the reaction mixture, for which the TM sustainability will be critical to keep the reaction rate constant. Furthermore, we intend to encapsulate Nox^m, catalase, and pTMe together in a silica shell in a future study to examine the effects of clustering of the reaction mixture on the TM sustainability.

Conclusion

Methods to improve the sustainability of in vitro NADPH generation by TMs have been extensively examined for improving vesicle utilization in biosynthetic reactions. The sustainability of NADPH generation in the TM can be extended via silica encapsulation. However, further removal of ROS by maintaining LEF in the presence of catalase is required to improve sustainability. Thus, if ROS formation by TM under light is properly suppressed or removed, it can be used to provide reducing power in vitro.

Supplementary Information

The online version contains supplementary material available at https://doi.org/10.1186/s12934-022-01825-1.

Additional file 1. Sustainability of in vitro light-dependent NADPH generation by the thylakoid membrane of *Synechocystis* sp. PCC6803. Table S1. PCR primers used in this study. Fig. S1. Determination of binding capacity of Ni-NTA and streptavidin resins for $TM_{\beta\text{-his}}$ and $TM_{c\text{-strep}}$. Fig. S2. NADPH and ATP generation activities of TM in light and dark. Fig. S3. Optimization

of FNR, Fd and phycobilisome (PBS) for the NADPH generation by TM. Fig. S4. Determination of PBS contents of cell-free extract, TM, and PBS-reconstituted TM (pTM). Fig. S5. ATP generation rate of pTM in the presence of FCCP. Fig. S6. Characterization of TM treated with varying concentrations of EDTA. Fig. S7. Determination of PBS contents of TM treated with 10 mM EDTA (TMe), and TMe reconstituted for PBS (pTMe). Fig. S8. Optimization of R5 and TMOS for the biosilicification of pTMe. Fig. S9. Microscopic observation of pTMe and b-pTMe. Fig. S10. Zeta potentials of pTMe, R5-pretreated pTMe, and b-pTMe. Fig. S11. Stability of the four major photosynthetic proteins of pTMe and b-pTMe during incubation at 30℃ in the dark. Fig. S12. Stability of the four major photosynthetic proteins of pTMe and b-pTMe during incubation at 30℃ in light. Fig. S13. Use of Synechocystis cell lysate for esterase activity and chloroform for lysis of pTMe and b-pTMe. Fig. S14. Determination of ROS generated by pTMe and b-pTMe. Fig. S15. Determination of antioxidant activity of R5. Fig. S16. Lineweaver-Burk plot (v_0^{-1} vs. $[NADPH]^{-1}$) illustrating the kinetic parameters of Nox^m. Fig. S17. General ROS generated from b-pTMe at 30℃ in light in the presence of SOD and catalase.

Acknowledgements
We would like to thank Editage (www.editage.co.kr) for English language editing.

Authors' contributions
JKL and EJK conceived of the study. XT performed the experiments. XT, EJK, and JKL analyzed the data. XT, EJK, and JKL wrote the manuscript. All authors have read and approved the final manuscript.

Funding
This study was supported by the National Research Foundation of Korea grants (2019R1F1A1061639 and 2019R1A2C2089870) funded by the Ministry of Science and ICT, and a grant (NNIBR2021021013) from the Nakdonggang National Institute of Biological Resources funded by the Ministry of Environment of the Republic of Korea.

Availability of data and materials
All data generated or analyzed during this study are included in this article and its additional files.

Declarations

Ethics approval and consent to participate
Not applicable.

Consent for publication
Not applicable.

Competing interests
The authors declare that they have no competing interests.

Received: 13 February 2022 Accepted: 15 May 2022
Published online: 28 May 2022

References

1. Van De Meene AML, Hohmann-Marriott MF, Vermaas WFJ, et al. The three-dimensional structure of the cyanobacterium *Synechocystis* sp. PCC 6803. Arch Microbiol. 2006;184(5):259–70.
2. Liberton M, Berg RH, Heuser J, Roth R, Pakrasi HB. Ultrastructure of the membrane systems in the unicellular cyanobacterium *Synechocystis* sp. strain PCC 6803. Protoplasma. 2006;227(2):129–38.
3. Mullineaux CW. Co-existence of photosynthetic and respiratory activities in cyanobacterial thylakoid membranes. Biochim Biophys Acta-Bioenerg. 2014;1837(4):503–11.
4. Kirchhoff H. Diffusion of molecules and macromolecules in thylakoid membranes. Biochim Biophys Acta-Bioenerg. 2014;1837(4):495–502.
5. Shikanai T. Cyclic electron transport around photosystem I: genetic approaches. Annu Rev Plant Biol. 2007;58:199–217.
6. Shikanai T. Regulation of photosynthesis by cyclic electron transport around photosystem I. Adv Bot Res. 2020;96:177–204.
7. Casella S, Huang F, Mason D, Zhao G, Johnson GN, Mullineaux CW, et al. Dissecting the native architecture and dynamics of cyanobacterial photosynthetic machinery. Mol Plant. 2017;10(11):1434–48.
8. Blackwell M, Gibas C, Gygax S, Roman D, Wagner B. The plastoquinone diffusion coefficient in chloroplasts and its mechanistic implications. Biochim Biophys Acta-Bioenergetics. 1994;1183(3):533–43.
9. Li M, Ma J, Li X, Sui SF. In situ cryo-et structure of phycobilisome–photosystem ii supercomplex from red alga. Elife. 2021;10: e69635.
10. Van Thor JJ, Geerlings TH, Matthijs HCP, Hellingwerf KJ. Kinetic evidence for the PsaE-dependent transient ternary complex photosystem I/ferredoxin/ferredoxin:NADP+ reductase in a cyanobacterium. Biochemistry. 1999;38(39):12735–46.
11. Miller TE, Beneyton T, Schwander T, Diehl C, Girault M, Mclean R, et al. Light-powered CO2 fixation in a chloroplast mimic with natural and synthetic parts. Science. 2020;368(6491):649–54.
12. Li F, Wei X, Zhang L, Liu C, You C, Zhu Z. Installing a green engine to drive an enzyme cascade: a light-powered in vitro biosystem for poly (3-hydroxybutyrate) synthesis. Angew Chemie. 2022;61(1): e202111054.
13. Yacoby I, Pochekailov S, Toporik H, Ghirardi ML, King PW, Zhang S. Photosynthetic electron partitioning between [FeFe]-hydrogenase and ferredoxin: NADP+-oxidoreductase (FNR) enzymes in vitro. Proc Natl Acad Sci. 2011;108(23):9396–401.
14. Kim H, Tong X, Choi S, Lee JK. Characterization of ATPase activity of free and immobilized chromatophore membrane vesicles of Rhodobacter sphaeroides. J Microbiol Biotechnol. 2017;27(12):2173–9.
15. Phoenix VR, Konhauser KO, Adams DG, Bottrell SH. Role of biomineralization as an ultraviolet shield: implications for archean life. Geology. 2001;29(9):823–6.
16. Iwai S, Doi K, Fujino Y, Nakazono T, Fukuda K, Motomura Y, et al. Silica deposition and phenotypic changes to Thermus thermophilus cultivated in the presence of supersaturated silicia. ISME J. 2010;4(6):809–16.
17. Phoenix VRKK. Benefits of bacterial biomineralization. Geobiology. 2008;6(3):303–8.
18. Wysokowski M, Jesionowski T, Ehrlich H. Biosilica as a source for inspiration in biological materials science. Am Mineral J Earth Planet Mater. 2018;103(5):665–91.
19. Yang SH, Lee K, Kong B, Kim J, Kim H, Choi IS. Biomimetic encapsulation of individual cells with silica. Angew Chemie Int Ed. 2009;48(48):9160–3.
20. Xiong W, Yang Z, Zhai H, Wang G, Xu X, Ma W, et al. Alleviation of high light-induced photoinhibition in cyanobacteria by artificially conferred biosilica shells. Chem Commun. 2013;49(68):7525–7.
21. Xiong W, Zhao X, Zhu G, Shao C, Li Y, Ma W, et al. Silicification-induced cell aggregation for the sustainable production of H2 under aerobic conditions. Angew Chemie. 2015;54(41):11961–5.
22. Perullini M, Orias F, Durrieu C, Jobbágy M, Bilmes SA. Co-encapsulation of Daphnia magna and microalgae in silica matrices, a stepping stone toward a portable microcosm. Biotechnol Reports. 2014;4:147–50.
23. Nassif N, Bouvet O, Rager MN, Roux C, Coradin T, Livage J. Living bacteria in silica gels. Nat Mater. 2002;1(1):42–4.
24. Luckarift HR, Johnson GR. Silica-immobilized enzyme reactors; application to cholinesterase-inhibition studies. J Chromatogr B. 2006;843(2):310–6.
25. Begarani F, Cassano D, Margheritis E, Marotta R, Cardarelli F, Voliani V. Silica-based nanoparticles for protein encapsulation and delivery. Nanomaterials. 2018;8(11):886.
26. Bialas F, Becker CFW. Biomimetic silica encapsulation of lipid nanodiscs and β-sheet-stabilized diacylglycerol kinase. Bioconjug Chem. 2021;32(8):1742–52.
27. Xiong Y, Ford NR, Hecht KA, Roesijadi G, Squier TC. Dynamic stabilization of expressed proteins in engineered diatom biosilica matrices. Bioconjug Chem. 2016;27(5):1205–9.
28. Tadaki D, Yamaura D, Araki S, Yoshida M, Arata K, Ohori T. Mechanically stable solvent-free lipid bilayers in nano-and micro-tapered apertures for reconstitution of cell-free synthesized hERG channels. Sci Rep. 2017;7(1):17736.
29. Khorobrykh S, Havurinne V, Mattila H. Oxygen and ROS in Photosynthesis. Plants. 2020;9(1):91.

30. Allen JF. Cyclic, pseudocyclic and noncyclic photophosphorylation: new links in the chain. Trends Plant Sci. 2003;8(1):15–9.
31. Heber U. Irrungen, wirrungen? The Mehler reaction in relation to cyclic electron transport in C3 plants. Photosynth Res. 2002;73(1–3):223–31.
32. Resnick SM, Zehnder AJB. In vitro ATP regeneration from polyphosphate and AMP by polyphosphate:AMP phosphotransferase and adenylate kinase from Acinetobacter johnsonii 210A. Appl Environ Microbiol. 2000;66(5):2045–51.
33. Sun C, Li Z, Ning X, Xu W, Li Z. In vitro biosynthesis of ATP from adenosine and polyphosphate. Bioresour Bioprocess. 2021;8(1):1–10.
34. Park JT, Hirano J, Thangavel V, Riebel BR, Bommarius AS. NAD(P)H oxidase V from Lactobacillus plantarum (NoxV) displays enhanced operational stability even in absence of reducing agents. J Mol Catal B Enzym. 2011;71(3–4):159–65.
35. Kim E, Kim J, Rhee HJ, Lee JK. Growth arrest of *Synechocystis* sp. PCC6803 by superoxide generated from heterologously expressed Rhodobacter sphaeroides chlorophyllide a reductase. FEBS Lett. 2009;583(1):219–23.
36. Tong X, Oh EK, Lee B-H, Lee JK. Production of long-chain free fatty acids from metabolically engineered Rhodobacter sphaeroides heterologously producing periplasmic phospholipase A2 in dodecane-overlaid two-phase culture. Microb Cell Fact. 2019;18(1):20.
37. Rodolfo WN, Yinsheng Z, Pakrasi HA. PhrA, the major photoreactivating factor in the cyanobacterium *Synechocystis* sp. strain PCC 6803 codes for a cyclobutane-pyrimidine-dimer-specific DNA photolyase. Arch Microbiol. 2000;173(56):412–7.
38. Lichtenthaler K. Chlorophylls and carotenoids: pigments of photosynthetic biomembranes. Methods Enzymol. 1987;148:350–82.
39. Berhanu S, Ueda T, Kuruma Y. Artificial photosynthetic cell producing energy for protein synthesis. Nat Commun. 2019;10(1):1325.
40. Yamanaka G, Glazer AN, Williams RC. Cyanobacterial phycobilisome. Characterization of the phycobilisomes of *Synechococcus* sp 6301. J Biol Chem. 1978;253(22):8303–10.
41. Bennett ABL. Complementary chromatic adaptation in a filamentous blue-green alga. J Cell Biol. 1973;58(2):419–35.
42. Baccarini-Melandri A, Gest H, Pietro AS. A coupling factor in bacterial photophosphorylation. J Biol Chem. 1970;245(5):1224–6.
43. Engelbrecht S, Althoff G, Junge W. Reconstitution of photophosphorylation in EDTA-treated thylakoids by added chloroplast coupling factor 1 (ATPase) and chloroplast coupling factor 1 lacking the δ subunit. Structural or functional? Eur J Biochem. 1990;189(1):193–7.
44. Wakayama T, Kato Y, Utsumi R, Tsuji A, Iseki S. A time-and cost-saving method of producing rat polyclonal antibodies. Acta Histochem Cytochem. 2006;39(3):79–87.
45. Kobayashi K, Osawa Y, Yoshihara A, et al. Relationship between glycerolipids and photosynthetic components during recovery of thylakoid membranes from nitrogen starvation-induced attenuation in *Synechocystis* sp. PCC 6803. Front Plant Sci. 2020;11:432.
46. Ha K, Baek K, Ki M, Ho S, Pil S. Novel silica forming peptide, RSGH, from Equus caballus: Its unique biosilica formation under acidic conditions. Biochem Eng J. 2020;153: 107389.
47. Chen H, Muramoto K, Yamauchi F, Fujimoto K. Antioxidative properties of histidine-containing peptides designed from peptide fragments found in the digests of a soybean protein. J Agric Food Chem. 1998;46(1):49–53.
48. Chen H, Muramoto K, Yamauchi F. Structural analysis of antioxidative peptides from Soybean. Beta.-Conglycinin. J Agric Food Chem. 1995;43(3):574–8.
49. Rodriguez SA, Murray AP, Leiro JM. Xanthine oxidase inhibition by aqueous extract of Limonium brasiliense (Plumbaginaceae). Chem Proceedings Multidiscip Digit Publ Inst. 2021;3(1):123.
50. Ruch RJ, Cheng Jun S, Klaunig JE. Prevention of cytotoxicity and inhibition of intercellular communication by antioxidant catechins isolated from chinese green tea. Carcinogenesis. 1989;10(6):1003–8.
51. Kim H, Kim H, Lee JK. Biochemical characterization of protoporphyrinogen dehydrogenase and protoporphyrin ferrochelatase of Vibrio vulnificus and the critical complex formation between these enzymes. Biochim Biophys Acta-Gen Subj. 2018;1862(12):2674–87.
52. Cheng Y, Zheng R, Wu X, Xu K, Song P, Wang Y, et al. Thylakoid membranes with unique photosystems used to simultaneously produce self-supplying oxygen and singlet oxygen for hypoxic tumor therapy. Adv Healthc Mater. 2021;10(6): e2001666.
53. Prasad A, Sedlářová M, Pospíšil P. Singlet oxygen imaging using fluorescent probe Singlet Oxygen Sensor Green in photosynthetic organisms. Sci Rep. 2018;8:1–13.
54. Elena Z, Norling B, Andersson B, Pakrasi HB. Subcellular localization of the BtpA protein in the cyanobacterium *Synechocystis* sp. PCC 6803. Eur J Biochem. 1999;261(1):311–6.
55. Kashino Y, Inoue-Kashino N, Roose JL, Pakrasi HB. Absence of the PsbQ protein results in destabilization of the PsbV protein and decreased oxygen evolution activity in cyanobacterial photosystem II. J Biol Chem. 2006;281(20):20834–41.
56. Fourmond V, Lagoutte B, Se P, Leibl W, Demaille C, Gif YV, et al. Electrochemical study of a reconstituted photosynthetic electron-transfer chain. J Am Chem Soc. 2007;129(29):9201–9.
57. Slovacek REHG. Correlation between photosynthesis and the transthylakoid proton gradient. Biochim Biophys Acta-Bioenergetics. 1981;635(2):393–404.
58. Shikanai T, Yamamoto H. Contribution of cyclic and pseudo-cyclic electron transport to the formation of proton motive force in chloroplasts. Mol Plant. 2017;10(1):20–9.
59. Konno H, Nakane T, Yoshida M, Ueoka-Nakanishi H, Hara S, Hisabori T. Thiol modulation of the chloroplast ATP synthase is dependent on the energization of thylakoid membranes. Plant Cell Physiol. 2012;53(4):626–34.
60. Brennan JP, Southworth R, Medina RA, Davidson SM, Duchen MR, Shattock MJ. Mitochondrial uncoupling, with low concentration FCCP, induces ROS-dependent cardioprotection independent of KATP channel activation. Cardiovasc Res. 2006;72(2):313–21.
61. Han YH, Yang YM, Park WH. Carbonyl cyanide p-(trifluoromethoxy) phenylhydroazone induces caspase-independent apoptosis in As4. 1 juxtaglomerular cells. Anticancer Res. 2010;30(7):2863–8.
62. Moroneys JV, Mccarty RE. Light-dependent cleavage of the gamma subunit of coupling factor 1 by trypsin causes activation of Mg2+-ATPase activity and uncoupling of photophosphorylation in spinach chloroplasts. J Biol Chem. 1982;257(10):5915–20.
63. Mccallum JR, Mccarty RE. Proton flux through the chloroplast ATP synthase is altered by cleavage of its gamma subunit. Biochim Biophys Acta-Bioenergetics. 2007;1767(7):974–9.
64. Mullineaux CW. Phycobilisome-reaction centre interaction in cyanobacteria. Photosynth Res. 2008;95(2–3):175–82.
65. Redlinger TGE. A Mr 95,000 polypeptide in Porphyridium cruentum phycobilisomes and thylakoids: possible function in linkage of phycobilisomes to thylakoids and in energy transfer. Proc Natl Acad Sci. 1982;79(18):5542–6.
66. Kale R, Hebert AE, Frankel LK, Sallans L, Bricker TM. Amino acid oxidation of the D1 and D2 proteins by oxygen radicals during photoinhibition of Photosystem II. Proc Natl Acad Sci. 2017;114(11):2988–93.
67. Lechner CC, Becker CFW. A sequence-function analysis of the silica precipitating silaffin R5 peptide. J Pept Sci. 2014;20(2):152–8.
68. Yu L, Chen Y, Lin H, Du W, Chen H, Shi J. Ultrasmall mesoporous organosilica nanoparticles: Morphology modulations and redox-responsive biodegradability for tumor-specific drug delivery. Biomaterials. 2018;161:292–305.
69. Gisbert-garzar M. Redox-Responsive Mesoporous Silica Nanoparticles for Cancer Treatment: Recent Updates. Nanomaterials. 2021;11(9):2222.
70. Xu P, Zheng Y, Zhu X, Li S, Zhou C. L-lysine and L-arginine inhibit the oxidation of lipids and proteins of emulsion sausage by chelating iron ion and scavenging radical. Asian-Australasian J Anim Sci. 2018;31(6):905–13.
71. Martin-Rubio AS, Sopelana P, Nakashima F, Shibata T, Uchida K, Guillén MD. A dual perspective of the action of lysine on soybean oil oxidation process obtained by combining 1H NMR and LC-MS: Antioxidant effect and generation of Lysine-Aldehyde adducts. Antioxidants. 2019;8(9):326.
72. Mubarakshina MM, Ivanov BN. The production and scavenging of reactive oxygen species in the plastoquinone pool of chloroplast thylakoid membranes. Physiol Plant. 2010;140(2):103–10.
73. Zhang Q, Padayatti PS, Leung JH. Proton-translocating nicotinamide nucleotide transhydrogenase: a structural perspective. Front Physiol. 2017;8:1089.
74. Eraso JM, Kaplan S. prrA, a putative response regulator involved in oxygen regulation of photosynthesis gene expression in Rhodobacter sphaeroides. J Bacteriol. 1994;176(1):32–43.

75. © 19 8 3 Nature Publishing Group http://www.nature.com/naturebiotechnology.

Publisher's Note